Industrial applications

Struct Multidisc Optim 28, 55–68 (2004)
DOI 10.1007/s00158-004-0437-5

Robust shape optimization of notches for fatigue-life extension

M. McDonald and M. Heller

Abstract An iterative 2D finite-element-based optimization procedure has been developed which incorporates robust design philosophies. This has been used to determine precise free-form shapes for a hole in a plate example, with the aim of maximizing its fatigue-life when exposed to varying load orientations. Past methods have typically considered only a single nominal load orientation, with empirical approaches to deal with the orientation variability, thus resulting in suboptimal solutions. Here a robust stress method is developed that produces a notch shape that minimizes the peak stress and renders it constant for a range of load orientations. Furthermore, a more sophisticated robust fatigue-damage optimization method is then developed to minimize the peak fatigue damage for a given stochastic distribution of load orientations. Fatigue calculations for an example problem with significant load orientation variation show that the robust optimization methods provide fatigue-life extensions 2 to 8 times better than past methods. It is anticipated that the implementation of robust optimal shapes in metallic components would result in greater fatigue-life extension.

Key words fatigue life enhancement, shape optimization, stress concentration

1 Introduction

A significant aspect of economic management of aging aircraft is fatigue-life evaluation and fatigue-life extension of metallic structures containing stress-concentrating features. An example of particular relevance to the Royal Australian Air Force is the internal fuel flow vent hole in the F-111 airframe (Fig. 1(a)), which is prone to fatigue cracking. Sometimes just a few of these stress concentrators, termed herein as notches, can govern the economic life of the airframe. Hence the development of fatigue-optimal shapes for such notches can realize significant gains: firstly by extending the life of the air vehicle, and secondly by reducing the cost of monitoring and repairing locations where fatigue cracking occurs.

A very important aspect to consider when determining optimal shapes is their robustness to varying condi-

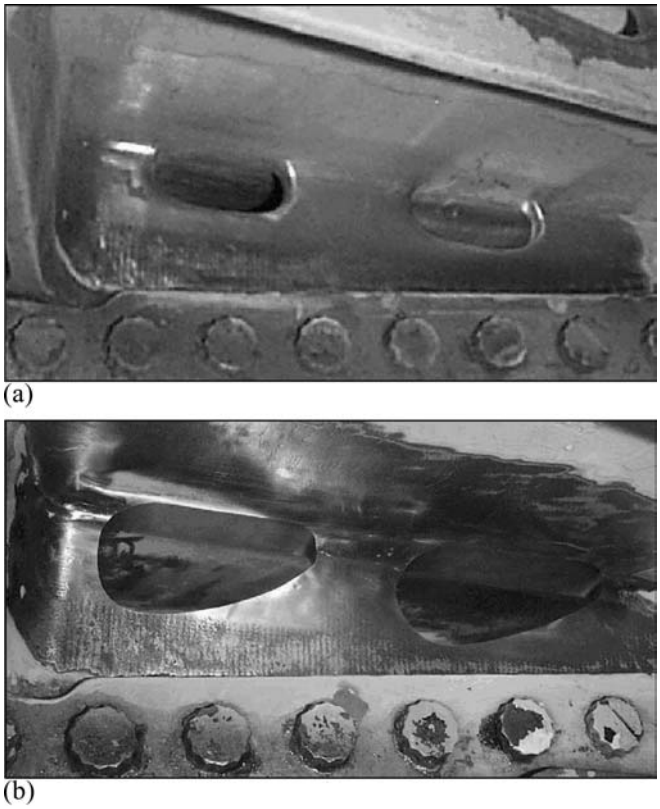

Fig. 1 Inside view of the F-111 wing pivot fitting showing fuel flow vent hole features where fatigue cracking typically occurs, showing (a) the original geometry, and (b) typical optimal shapes (Heller *et al.* 2001)

Received: 17 February 2003
Revised manuscript received: 30 March 2004
Published online: 8 July 2004

M. McDonald✉ and M. Heller

Defence Science and Technology Organisation, 506 Lorimer Street, Fishermans Bend, Victoria, 3207, Australia
e-mail: marcus.mcdonald@dsto.defence.gov.au

tions. Conditions that can vary include: magnitude and orientation of in-service loads; manufacture tolerances; build quality; and numerical modelling approximations and errors. Consider a typical scenario where a shape is optimized to give maximum fatigue-life using an idealized set of nominal conditions. It can reasonably be expected that any perturbation from these nominal conditions is likely to result in suboptimal performance.

For example, this concern has recently been demonstrated in prior work on managing fatigue cracking at the fuel flow vent holes in the F-111. Optimal shapes were determined for these holes as shown in Fig. 1(b) (Heller *et al.* 2001). The shapes were optimized to reduce the stress concentration factor (K_t) for a single dominant loading condition (compare Fig. 2(a) and (b)). A sensitivity study revealed that when worst-case loading variations and manufacture tolerances were modelled, the K_t would increase by as much as 15% (see Fig. 2(c), McDonald *et al.* 2001). In order to limit this stress increase within an acceptable level, very tight position tolerances were imposed on the optimal shapes. This placed a significant obligation on the manufacturers to improve the accuracy of the machining process, thus increasing implementation costs. Clearly it would have been preferable to modify the optimal shape instead, in order to decrease the sensitivity to load orientation, so that the machining tolerances could have been more relaxed.

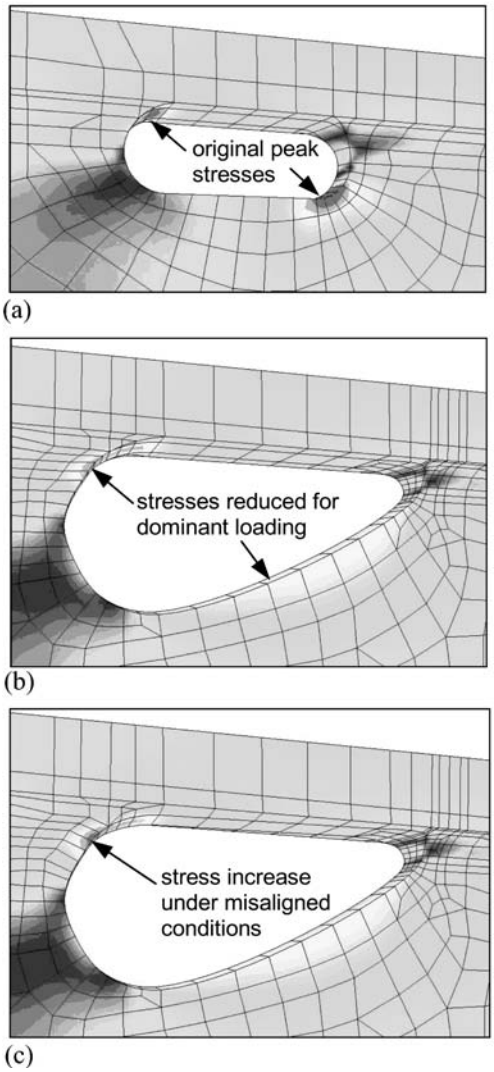

Fig. 2 Stress contours about a typical fuel flow vent hole in the F-111 wing pivot fitting structure with (a) the original shape, (b) a typical optimized shape under nominal conditions (Heller *et al.* 2001), and (c) the same optimized shape under conditions varied away from nominal (McDonald *et al.* 2001)

This raises the question, can the shape of a notch be optimized to give a long fatigue-life for a range of conditions, rather than just a single nominal condition. In the context of managing a fleet of airframes, this could realize significant benefits such as: reduced machining costs; a common **robust** optimal notch shape for several airframe variants; improved reliability of residual life assessments; and longer fatigue-life extension. Although the context of this work is the life extension of existing structures, it is also completely applicable to the design of new structures.

2
Robust optimal shapes for fatigue

2.1
Prior work

There are three disciplines of interest here: robust optimization methods for a continuous range of loading scenarios, fatigue and probabilistic considerations.

To the authors' knowledge, no published works are available where the peak stresses around a notch boundary segment are rendered completely constant for a continuous range of loading scenarios. However there are some works that produce notch shapes where the same peak stress is achieved for a number of distinct load cases (Kristensen and Madsen 1976; Xie and Steven 1992; and Herskovits *et al.* 1996). While these multiple load case shapes have relevance to the present work, they do not specifically address a continuous range of loading conditions, and they do not address fatigue or stochastic issues.

Optimization of notches for fatigue has been studied extensively. For example, Fanni *et al.* (1994) developed optimal shapes for notches in machine components based on minimization of the fatigue notch factor (K_f). Further work by Grunwald and Schnack (1997) approached similar problems using a continuum damage mechanics model. More recent work by Chaperon *et al.* (2000) approaches the optimization problem using fracture mechanics criteria. However, none of these works address the issue of robustness, i.e. they are all developed for a single loading condition only.

The design of general structures (typically layouts) with probabilistic consideration of uncertainties is well established (Phadke 1989; Taguchi *et al.* 1989). More re-

cently, the issue of uncertainties has been merged into general structural optimization procedures and is commonly referred to as either: stochastic or probabilistic optimization, reliability optimization, or more simply, robust optimization (Rao 1979; Parkinson *et al.* 1993; Chandu and Grandhi 1995; Melchers 2001). Although there are already a large number of papers dealing with this issue, it appears that these techniques have not yet been applied to the area of precise free-form shape optimization of notches, nor have they been combined with fatigue models.

Hence the most pertinent technology gap in all of the above works is not the lack of expertise in any one particular area. It is the incomplete amalgamation of these technologies to create a simple but comprehensive robust shape optimization procedure for fatigue-life extension of notches. Hence in this paper, the issues of robustness, fatigue-life and stochastic effects are brought together with precise free-form shape optimization in an attempt to close this technology gap.

2.2 Outline of present work

Firstly, a straightforward stress-based shape optimization method for single load cases is briefly described in Sect. 3, since it is the baseline procedure for further development. In Sect. 4.1, this procedure is extended to deal with a continuous range of load cases, with the aim of determining a notch shape such that the peak stress is not only minimized, but is also rendered completely constant over the range of cases. The goal of maximizing the fatigue-life is then addressed in Sect. 4.2, through incorporation of a typical fatigue model into the procedure. Here the aim is to minimize the peak fatigue-damage accumulated at the notch boundary, while also accounting for probabilistic loading effects.

An example problem definition consisting of a hole in a large plate is described in Sect. 5, which is used to benchmark the baseline procedure in Sect. 6. Then, the example problem is used to illustrate the effectiveness of each development of the robust optimization procedure, which are given in Sects. 7, 8 and 9. These contain results of the example problem for: the baseline non-robust stress method; the robust stress method; and the robust fatigue-damage method respectively. There are no published solutions that the authors are aware of to compare the robust fatigue method results, however it will be illustrated by numerical example that the desired outcomes are achieved.

3 Basic stress optimization procedure for a single fixed loading condition

The basic stress optimization approach used here for subsequent further development is a gradient-less approach. It is used here since it is simple to implement, readily amenable to extension, and has been shown to achieve very good solutions for stress minimization, for realistic geometrically constrained problems under single load conditions. The typical quality of the solutions is discussed further in Sect. 6, which includes a sample benchmark problem. Further details can be found in Kaye and Heller (1997), and Waldman *et al.* (2001, 2002). Here we give an outline for completeness.

The present approach is based on the aim of achieving a minimum stress peak by directly attempting to make the stresses uniform along the longest segment of a boundary. This idea is well known, and some typical numerical approaches include those of Schnack (1979), Mattheck and Burkhardt (1990), and Kaye and Heller (1997). Analytical approaches using this aim include those of Baud (1934), Neuber (1969), and Vigdergauz and Cherkayev (1986). Experimental approaches include Heywood (1945). The different numerical algorithms are all useful and have various advantages and disadvantages in their implementation.

The present gradient-less shape optimization method involves iterative finite-element (FE) solutions to alter the local geometry to achieve a constant boundary stress. The general approach is to add material to regions of high stress and remove from regions of low stress. Consider a free boundary Γ on which there are a number of nodes $i = 1 \ldots k$, under an arbitrary remote loading, see Fig. 3(a). For an arbitrary (non-optimal) boundary shape, the tangential stress will generally vary along the boundary, as shown schematically in Fig. 3(b).

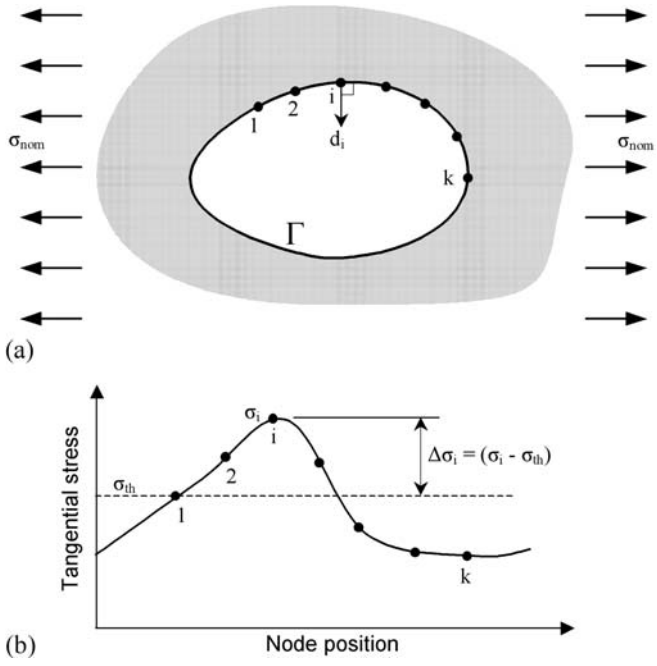

Fig. 3 Schematic to explain the gradient-less shape-optimization method for an arbitrary boundary segment: (a) geometric shape defined by k nodes on contour Γ; (b) tangential stress distribution along the boundary segment

The amount of material to be added or removed at any point on the boundary is taken in direct proportion to the difference between the local tangential stress and a suitable reference value. This process is repeated iteratively until the boundary stress is constant, or near constant to within a prescribed tolerance. For each iteration, the amount of movement (in the direction of the outward normal) for any given position i on the boundary is given by

$$d_i = \left(\frac{\sigma_i}{\sigma_{th}} - 1 \right) s \tag{1}$$

where d_i is the outward normal boundary movement, σ_i is the hoop stress at position i, σ_{th} is a non-zero threshold stress that is updated each iteration, and s is a step-size scaling factor (Kaye and Heller 1997). Each iteration material is added or removed at each position i depending on the chosen threshold stress. If the magnitude of the stress at position i is less than the magnitude of the threshold stress, then material is removed at this position. Otherwise, if it is greater, then material is added. Unlike some other gradient-less approaches, the present method is free-form, in the sense that the coordinates of neighbouring nodes on Γ are not defined by a prescribed function. This contributes to achieving precise, minimal stress solutions.

If desired, a minimum-radius constraint can be implemented by constraining the allowable movement of a node so that the radius of a three-point arc fitted through the node and its immediate neighbours is no less than a minimum value ρ (Waldman *et al.* 2002). This feature is typically only invoked at very localized regions on the notch boundary. A benchmark problem is solved using the basic stress method later in Sect. 6, following a description of the typical FE model.

4
Robust gradient-less optimization procedure for multiple loading conditions or load perturbations

4.1
Robust stress minimization method

The aim here is to determine a notch shape that renders the peak stress constant and minimal for a continuous range of load orientations. To explain how this might be achieved numerically, consider Fig. 4. This shows an arbitrary hole in a plate subject to a single remote uniaxial load, where the angular orientation α of that load can occur anywhere within a prescribed range. The range of load angles, which is considered to be continuous in practice, is discretized here into an appropriate number of individual load cases $l = 1 \ldots m$, where l is the load case identifier and m is the total number of cases. For an arbitrary initial hole shape, the stress distribution $\sigma_{i[l]}$ around the hole will usually be different for each load angle, as shown in Fig. 5. It can be seen that both the magnitude and position of the peak stress is typically different for each load case. Figure 5 also shows in bold the locus of the maximum peak stress

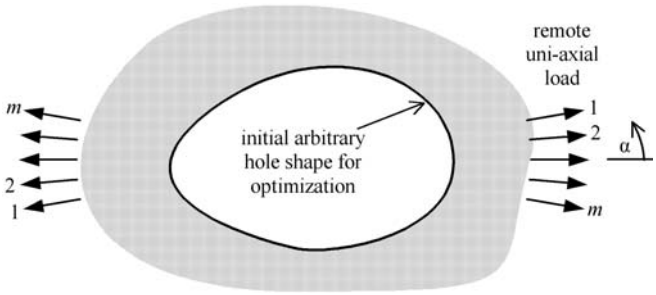

Fig. 4 Geometry and notation of an arbitrary hole in a plate under a remote uniaxial load with varying orientation α, showing the discretized load cases representing the continuous variation

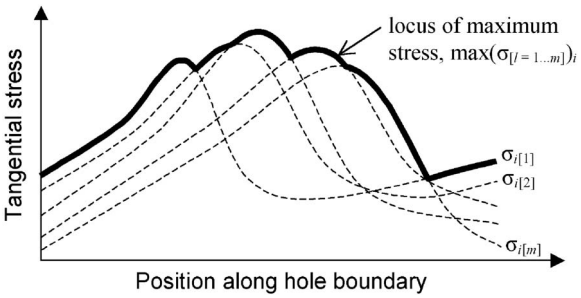

Fig. 5 Typical stress distributions about part of an arbitrary hole shape for different load condition cases, showing the locus of the maximum-stress distribution

distribution $\max(\sigma_{[l=1\ldots m]})_i$ of all the load cases. We want to make all stress peaks the same magnitude for all load cases, to achieve a locus of maximum stress that is uniform.

To implement this aim numerically, we can calculate the node movements in a similar fashion to the basic method (1) except here the stress term σ_i is replaced with the locus of maximum stress term $\max(\sigma_{[l]})_i$. Hence in each iteration the boundary node movements for the robust stress method are given by

$$d_i = \left(\frac{\max(\sigma_{[l]})_i}{\sigma_{th}} - 1 \right) s \tag{2}$$

where d_i is the node movement at position i, $\max(\sigma_{[l]})_i$ is the locus of maximum stress for all load cases at position i for load cases $l = 1 \ldots m$, σ_{th} is the non-zero threshold stress, and s is a step-size scale factor. The effectiveness of this procedure is demonstrated later in Sect. 8 by an illustrative example.

4.2
Robust fatigue-damage minimization method including probabilistic effects

We can now extend the approach given in the previous section to determine a notch shape that maximizes the fatigue-life, by rendering the accumulated fatigue-damage constant along the optimized notch boundary. Firstly though, the probabilistic effect of load angle occurrences is

discussed. It is considered that each time a load cycle is applied, the load orientation α occurs with some uncertainty, as shown schematically in Fig. 6. A normal distribution function was arbitrarily chosen in this work to describe the uncertainty, however any statistical distribution could be readily used.

As per the robust stress-minimization method described in the previous section, it is necessary to discretize this variation into a number of individual load cases $l = 1 \ldots m$. Then, the number of occurrences of each load case is calculated, which is then used later for fatigue-life calculations. The load case occurrences for a normal distribution function are given by the following,

$$n_{[l]} = n_{total} \left[\frac{1}{\sqrt{2\pi}\alpha_{stdev}} e^{-\left(\frac{(\alpha_{[l]} - \alpha_{avg})^2}{2\alpha_{stdev}^2} \right)} \right] \tag{3}$$

where α_{avg} and α_{stdev} are the average and standard deviation of the load-orientation distribution respectively, $\alpha_{[l]}$ is the discretized value of the orientation for each load case $l = 1 \ldots m$, and n_{total} is the total number of load cycles applied to the structure. This function is represented schematically in Fig. 7, which shows the idealized continuous load-occurrence distribution, along with a typical discretized distribution.

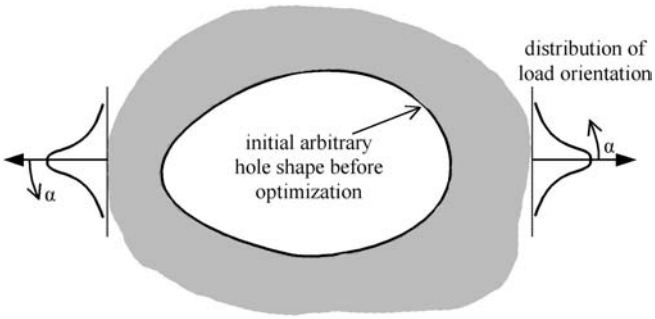

Fig. 6 Arbitrary hole in a plate under remote uniaxial constant-amplitude load cycles, where its angular orientation α varies each cycle in accordance with a normal distribution

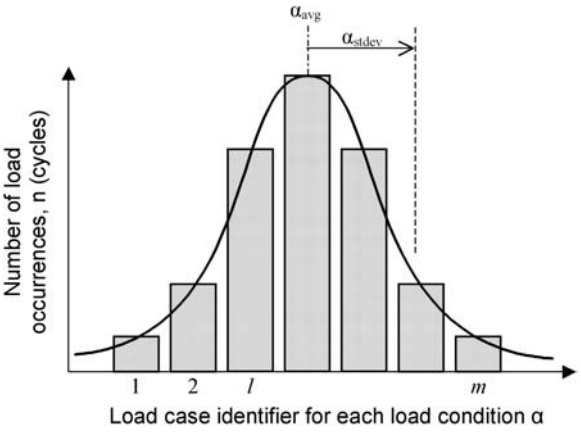

Fig. 7 Schematic of a load-occurrence normal distribution, showing the idealized continuous function and a typical discretized load-case distribution

This discretized distribution of load-case occurrence forms the basis for the fatigue-life calculations. It is important to consider that each position about the optimal boundary will experience a unique variable-amplitude stress history due to the various load-angle occurrences, hence an appropriate fatigue-damage rule needs to be selected that accounts for this.

In this paper a simple fatigue-life model is implemented known as the nominal stress (K_t) approach. It considers the free-boundary stress solution at each position along the notch boundary, and thus can be readily implemented in the existing gradient-less procedure with minimal programming effort. The fatigue life is calculated using the *linear cumulative-damage rule*, otherwise commonly known as the Miner rule (Miner 1945). It is a reasonable rule that still retains widespread use in most industries due to computational efficacy. The criterion for this rule states that fatigue failure will occur when

$$f = \sum_{j=1}^{c} \frac{n_j}{N_{fj}} \geq 1 \tag{4}$$

where f is the accumulated fatigue-damage, n_j is the number of cycles corresponding to the jth stress amplitude of $\Delta\sigma_j$, and N_{fj} is the number of cycles to failure for a constant amplitude of $\Delta\sigma_j$. The nominal stress approach is applied to the cumulative-damage rule via a simple linear log-log stress-life (S–N) relationship given as

$$\log_{10}(\Delta\sigma_j) = a.\log_{10}(N_{fj}) + b \tag{5}$$

where a and b are experimentally determined constants, and $\Delta\sigma_j$ is greater than an endurance stress limit σ_e. By rearranging (5), the number of cycles to failure for any given $\Delta\sigma_j$ can be calculated using the following

$$N_{fj} = \begin{cases} 10^{\left\lfloor \frac{\log_{10}(\Delta\sigma_j) - b}{a} \right\rfloor} & \text{if } \Delta\sigma_j \geq \sigma_e \\ \infty \text{ otherwise} \end{cases} \tag{6}$$

For the FE implementation the boundary movement at each node position i about the notch boundary is calculated the same way as the earlier stress-minimization method given in (1) or (2), except here the stress terms are replaced with fatigue-damage terms. For the non-robust (single load case) scenario, the boundary movement is given by the following formula

$$d_i = \left(\frac{f_i}{f_{th}} - 1 \right) s \tag{7}$$

where f_i is the accumulated fatigue-damage at position i calculated in accordance with (4), and f_{th} is a non-zero threshold fatigue-damage value which is applied in the same manner as the stress-minimization method described

earlier. For the robust (multiple load case) scenario, the boundary movement is given by

$$d_i = \left(\frac{\max \left(f_{[l]} \right)_i}{f_{th}} - 1 \right) s \tag{8}$$

where $\max(f_{[l]})_i$ is the maximum fatigue damage at position i for all load cases $l = 1 \ldots m$. The normal distribution of the multiple load cases is readily implemented within the fatigue-damage calculation by replacing the n_j term in (4) with $n_{[l]}$ as defined by (3). A numerical demonstration of the robust fatigue-damage minimization method is given later in Sect. 9.

4.3 General numerical implementation

The gradient-less method is highly suitable for implementation with any FE software that has a programming capability. Figure 8 shows a graphical flowchart of the simple iterative FE procedure. A fully automated procedure was implemented here using the pre- and post-processing software MSC.Patran$^{\mathrm{TM}}$, and the FE solver MSC.Nastran$^{\mathrm{TM}}$. It utilizes the MSC.Patran$^{\mathrm{TM}}$ command language (PCL), which can readily automate the iterative process. PCL can also perform some complex geometric and FE modelling functions (e.g. finding the intersection of complex curves and auto-free meshing), which are useful for ease of implementation.

The user starts with an FE model ready for analysis with all of the load cases $l = 1 \ldots m$ set up (typically in this work, $m = 1$ to 41 depending on the specific analysis case). A region of FE mesh about the optimized boundary is created (or recorded) parametrically using PCL. This mesh creation procedure is used later during the iterative process to create new boundary shapes automatically.

The iteration process begins by solving all individual load cases. Then, stress results are extracted along the optimal boundary for each case. If a robust fatigue-life optimization is being performed, then fatigue-damage quantities are calculated. Next, the convergence of the optimization is assessed. A useful parameter to monitor the convergence is the normalized range along the optimal boundary, as given by the equation

$$\Psi_\sigma = \frac{\max \left(\max \left(\sigma_{[l]} \right)_i \right) - \min \left(\max \left(\sigma_{[l]} \right)_i \right)}{\operatorname{avg} \left(\max \left(\sigma_{[l]} \right)_i \right)} \tag{9a}$$

for the stress-minimization method, and

$$\Psi_f = \frac{\max \left(\max \left(f_{[l]} \right)_i \right) - \min \left(\max \left(f_{[l]} \right)_i \right)}{\operatorname{avg} \left(\max \left(f_{[l]} \right)_i \right)} \tag{9b}$$

for the fatigue-damage-minimization method, where the max, min and avg notations refer to the maximum, minimum and average of the optimized quantities respectively along the optimal boundary (excluding minimum-radius regions and constraint edges). Clearly, as Ψ approaches zero, the stress or fatigue-damage distribution becomes more uniform along the boundary and the optimal shape is approached. Typically, a parameter of less than 0.002 (0.2%) was achieved in this work.

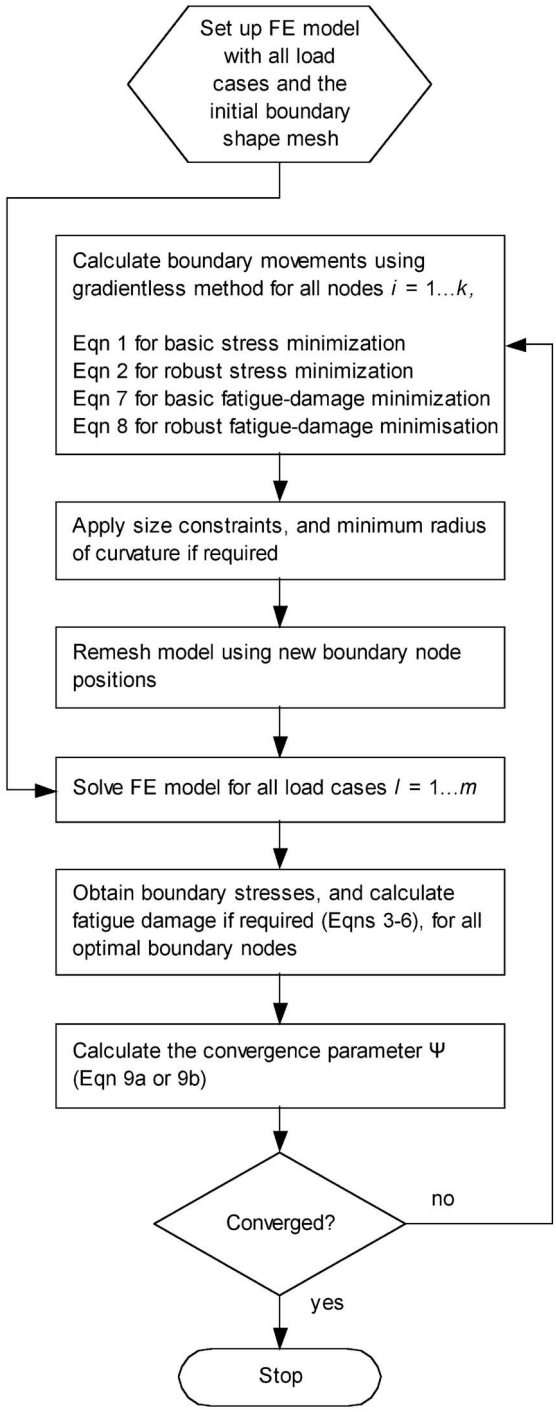

Fig. 8 Typical flow chart of the iterative finite-element implementation of the gradient-less shape-optimization method

If the optimization has not converged, a boundary movement is then performed. Node movements are calculated for all nodes along the optimal boundary. Either of the optimization methods can be implemented at this point, i.e. basic or robust stress minimization ((1) or (2)), or basic or robust fatigue-damage minimization ((7) or (8)).

Then the FE mesh region about the boundary is recreated using the mesh-creation PCL procedure noted above. Finally, all of the individual load cases are analysed again, and hence the process repeats until convergence is achieved. The procedure readily allows the addition and/or subtraction of material along the moving boundary. This is a 2D implementation, which may be readily transferred to $2^1/_2$D.

5 Geometry and load definition of the example problem

The example problem used in this work was a hole in a large plate, where the hole was geometrically constrained to have a prescribed height-to-length ratio of $H : L$ as shown in Fig. 9. The remote uniaxial stress σ_{nom} is nominally oriented at an inclination angle of $\alpha = 0°$. It is considered that this inclination angle may vary over a continuous range.

The finite-element model of the problem (Fig. 10) consists of rectangular 8-noded iso-parametric 2D plate elements with an arbitrary thickness of 1. A total of 46 corner nodes were modelled along each quarter of the hole boundary. A full model was created because the orientation of the uniaxial remote stress varies, even though the final optimal shape is expected to be symmetrical. The remote plate boundary is circular with radius $R_b = 10L$, which allowed the remote uniaxial stress to be easily applied at any desired inclination angle. This stress was applied via forces on the remote boundary nodes as shown in Fig. 10 for the nominal case.

The nodal forces that give a uniform remote stress can be derived from first principles based on the projected stress component on each element edge about the remote boundary. This is then distributed to the nodes keeping in mind that midside nodes require double the amount of force as corner nodes in order to maintain a uniform stress distribution. These equations are given below, showing the corner and midside nodal force magnitudes (x and y directions) respectively to give a uniform stress distribution of magnitude σ_{nom} for any uniaxial inclination angle α,

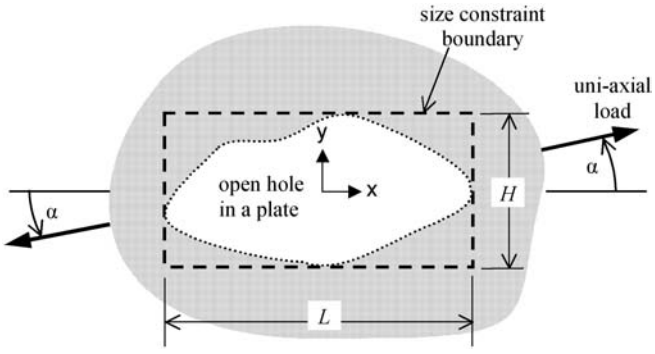

Fig. 9 Example problem of a size-constrained hole in a large plate under a remote uniaxial load

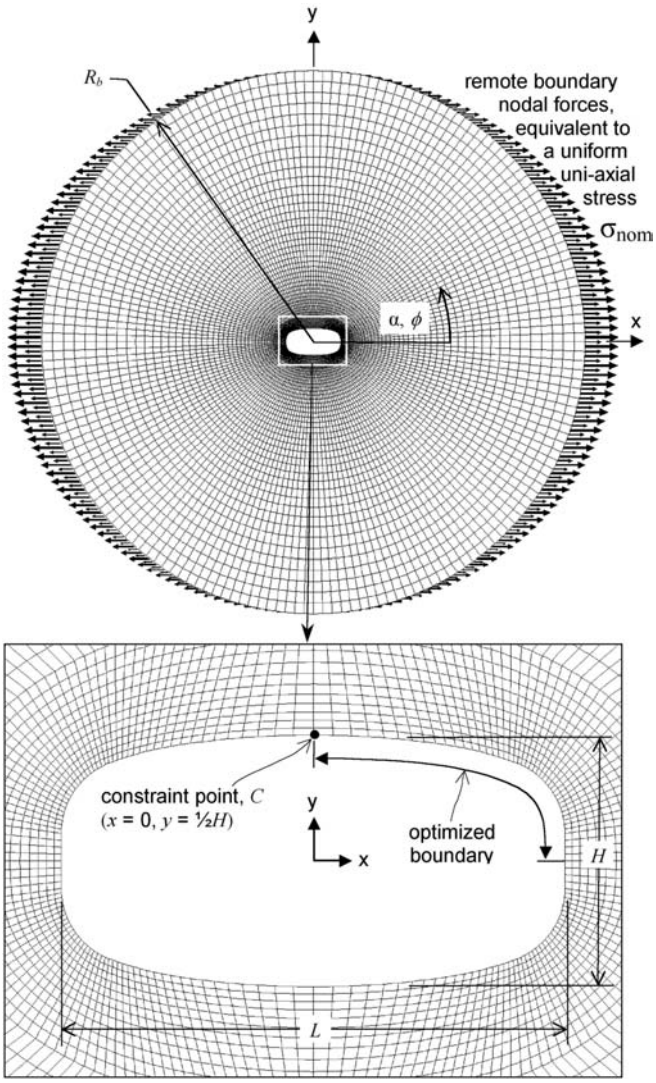

Fig. 10 Example view of the FE mesh for the hole-in-a-plate example problem, showing the remote uniaxial stress applied at the nominal inclination angle of $\alpha = 0°$

$$Fx(corner)_i = \frac{2}{3}\sigma_{nom} 2R_b \sin\left(\frac{\beta}{4}\right)\cos(\alpha - \phi_i)\cos(\alpha) \tag{10a}$$

$$Fy(corner)_i = \frac{2}{3}\sigma_{nom} 2R_b \sin\left(\frac{\beta}{4}\right)\cos(\alpha - \phi_i)\sin(\alpha) \tag{10b}$$

$$Fx(midside)_i = \frac{4}{3}\sigma_{nom} 2R_b \sin\left(\frac{\beta}{4}\right)\cos(\alpha - \phi_i)\cos(\alpha) \tag{11a}$$

$$Fy(midside)_i = \frac{4}{3}\sigma_{nom} 2R_b \sin\left(\frac{\beta}{4}\right)\cos(\alpha - \phi_i)\sin(\alpha) \tag{11b}$$

where β is the angular spacing between the remote boundary corner nodes ($\beta = 2°$ for this example) and ϕ_i is the

angular position of the remote boundary node. A number of separate load cases were applied to the remote boundary to cover the range of load inclination angles of interest, typically discretized into 1° increments. For all cases an arbitrary remote stress of $\sigma_{nom} = 1$ was applied.

Boundary node movements were only calculated for the upper-right quadrant of the model as indicated in Fig. 10, because the optimal shape solution is known to be symmetrical about the x and y axes for all of the analysed cases. The shape of the remaining three quadrants was maintained as mirror images of the first.

The size of the optimal shape was constrained to have a length of L and a height of H where $L = 2H$ (except for the benchmark case where $L = H$). Without these size constraints, the optimization would produce trivial solutions of either 'no hole', or an 'infinite slit', depending on whether material removal or addition was allowed. Choosing different aspect ratios will result in different unique optimal solutions as expected. An additional constraint point $C(x = 0, y = 1/2H)$ was also applied to prevent free-body movement. The stress threshold σ_{th} was always chosen to be equal to the stress at the constraint point C, and was updated each iteration. Material addition and subtraction were both allowed. Finally, the minimum-radius constraint $\rho = R_{min}/L$ was applied by restricting the movement of any given node such that the radius of a three-point arc passing through it and its two neighbours did not fall below a minimum radius R_{min}.

6
Benchmark case using the basic stress-minimization method

It is useful to demonstrate the effectiveness of the basic stress-optimization algorithm as used here; since it is the basis for further extension for robustness as described in Sect. 4. A typical hole benchmark is a constrained optimal hole in a plate subjected to a uniform uniaxial stress field (i.e. $\alpha = 0°$). Here the hole is constrained to have a 1 : 1 aspect ratio ($H = L$). A detailed analysis of this geometric case (amongst many others) was conducted by Burchill and Heller (2004b). Their analysis produced the lowest peak K_t, with $K_t = 2.18$ as compared to a number of other works including Durelli *et al.* (1979) with $K_t = 2.51$, Dhir (1981) with $K_t = 2.47$, and Schnack and Sporl (1986) with $K_t = 2.30$. Similar benefits of the present method for other benchmark problems, such as constrained shoulder fillets and plates with surface notches have been previously shown, see respectively, Waldman *et al.* (2003) and Burchill and Heller (2004a).

To be consistent with the Burchill and Heller (2004b) benchmark, the starting shape was a rhombus as shown in Fig. 11(a) and a minimum-radius constraint of $\rho = 0.15$ was used. The resulting optimal shape and stress distributions are given in Fig. 11(a) and (b) respectively, along with the Burchill and Heller (2004b) solution for comparison (using quarter symmetry). The shape of the optimal hole of the present implementation is virtually indistinguishable from the Burchill and Heller (2004b) solution, and both results produce the same peak K_t of 2.18, for $\Psi_\sigma < 0.1\%$. This is as desired, noting that both results were achieved using the same gradient-less stress-minimization method, with only some minor differences in implementation, but using two different FE codes.

Figure 12 shows the typical convergence of the present approach, for both the initial rhombus shape as well as for an initial circular shape. For example, 11 iterations were needed to achieve $\Psi_\sigma < 1.0\%$, when the starting shape was a circle and 44 iterations when it was a rhombus. For a similar convergence level the previous procedure of Burchill and Heller (2004b) required many more iterations, approximately 250, when starting from the rhombus. The reasons for this are that the prior method was restricted to material removal only, and thus required a small fixed step-size factor ($s = 0.007$) to avoid overshooting the op-

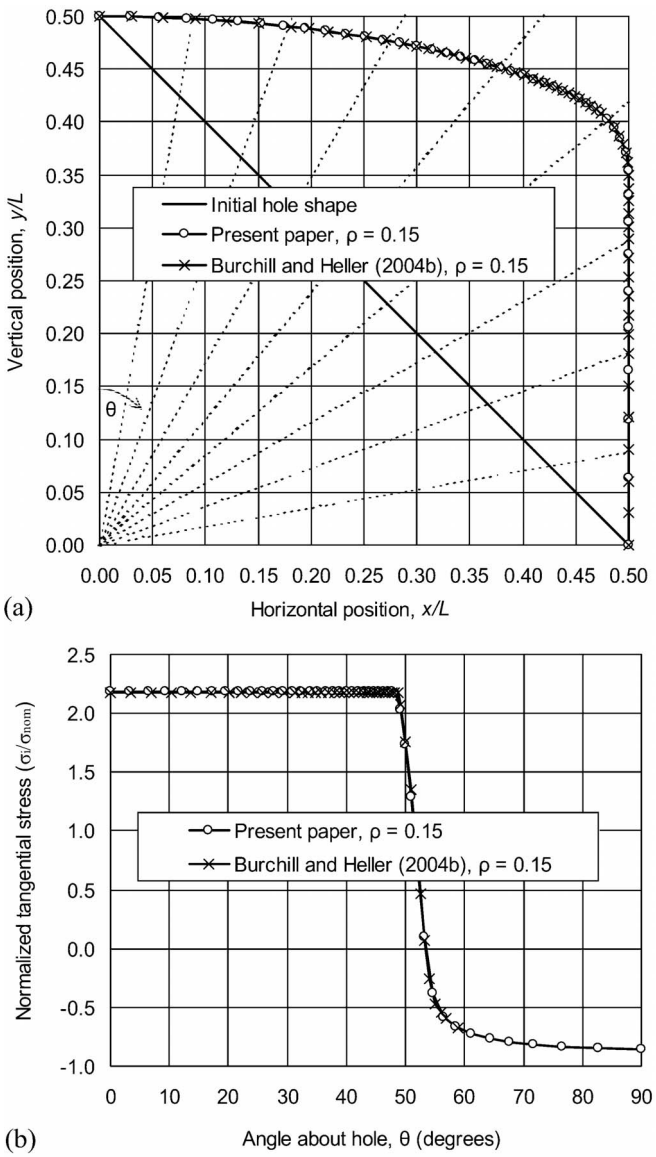

Fig. 11 Basic stress minimization results for the benchmark 1 : 1 shape-constrained optimal hole in a uniaxial stress field

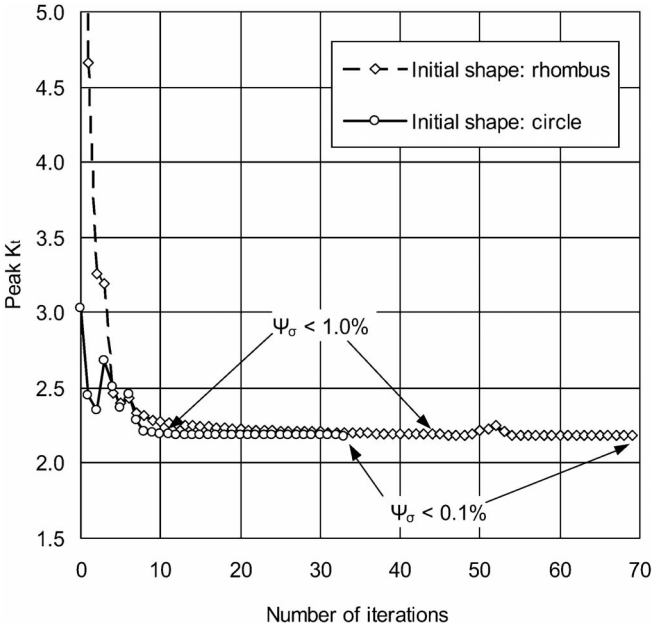

Fig. 12 Convergence of the peak K_t for the benchmark case, as a function of iteration number; two starting shapes are considered

timum boundary shape. Whereas the present numerical approach allowed material addition and subtraction, and used a variable s every iteration. The variable-s formulation was implemented by monitoring the convergence rate every iteration and is as yet unpublished, but it is not presented here as it is of no importance to the quality of the final stress results in this or subsequent sections.

As expected and shown in Fig. 12, the total number of iterations in the present method depends highly on the initial starting shape and the convergence tolerance. It would also depend to some extent on the specific element type used, but investigation of this issue is beyond the scope of the present paper.

7 Illustrative example for the non-robust stress-minimization method

Optimal shapes for the example 2 : 1 aspect ratio problem were determined using the basic gradient-less stress-minimization method, and are presented here in order to give baseline results for subsequent comparison. They

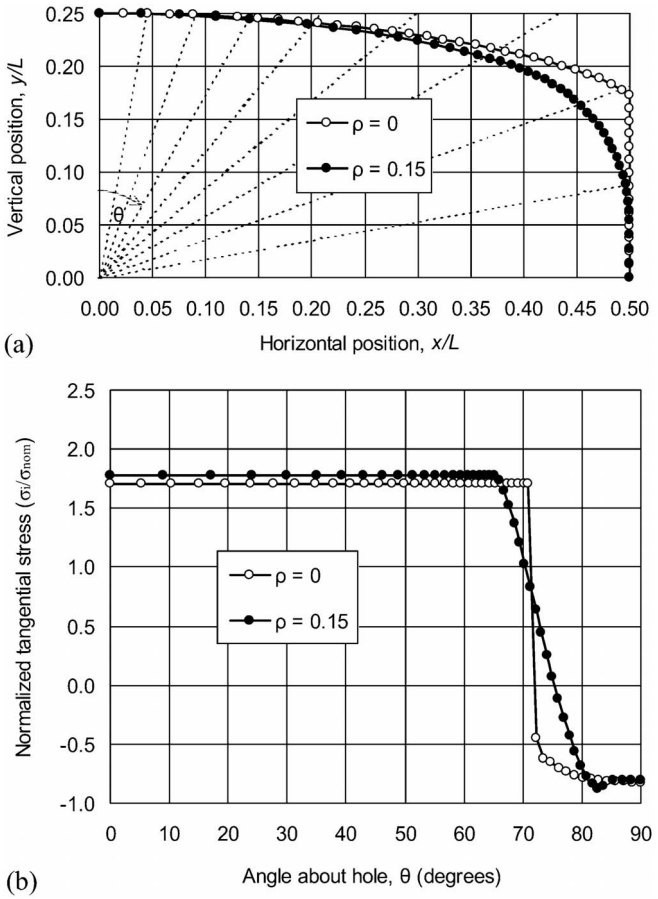

Fig. 13 Basic stress-minimization results with and without a minimum-radius constraint, showing (a) optimal hole shapes and (b) stress distributions about the hole boundaries when the load angle is at the nominal orientation of $\alpha = 0^\circ$

were optimized for the nominal load angle of $\alpha = 0^\circ$ only. Two shapes were determined, one without a minimum-radius constraint ($\rho = 0$) and one with a constraint of $\rho = 0.15$. Table 1 contains a summary of all results, including the convergence parameter Ψ_σ, which shows that all of the optimization cases converged to within 0.1%. Typically, each solution required 50 to 100 iterations to converge, where the starting shape was a $L \times 0.5L$ rectangle with rounded corners equal to the minimum-radius constraint.

The case with no minimum-radius constraint ($\rho = 0$) resulted in a shape containing sharp corners as shown in Fig. 13(a), as compared to the $\rho = 0.15$ case which has

Table 1 Summary of peak K_t results from the basic and robust stress-minimization methods for a 2 : 1 hole aspect ratio

Optimization method	Load-angle design range	Minimum-radius constraint ρ	Convergence parameter Ψ_σ	Peak stress-concentration factor K_t for various α (bold values represent optimal results)	
				$\alpha = 0^\circ$	$\alpha = \pm 5^\circ$
Basic stress minimization	$\alpha = 0^\circ$	0.0	0.08%	**1.71**	3.23
	$\alpha = 0^\circ$	0.15	0.05%	**1.78**	2.20
Robust stress minimization	$-5^\circ \le \alpha \le +5^\circ$	0.15	0.02%	**1.91**	**1.91**

a smooth transition from the optimal part of the boundary to the constraint edge. Figure 13(b) compares the stress distributions about the holes at the nominal load angle $\alpha = 0°$. As expected, the sharp corner ($\rho = 0$) case achieves the minimum peak K_t possible for the given example. The minimum-radius constraint causes a slight shortening of the length of the optimal part of the boundary, which has a slightly adverse affect on the minimum peak K_t that can be achieved.

It is useful now to demonstrate the effect that rotating the load angle α inclination has on the peak stress for these shapes. Figure 14 shows the stress distributions about the hole boundaries when the load is orientated at an $\alpha = 5°$ perturbation. The $\rho = 0$ case is most affected, with a significant increase in stress at the sharp corner, as expected.

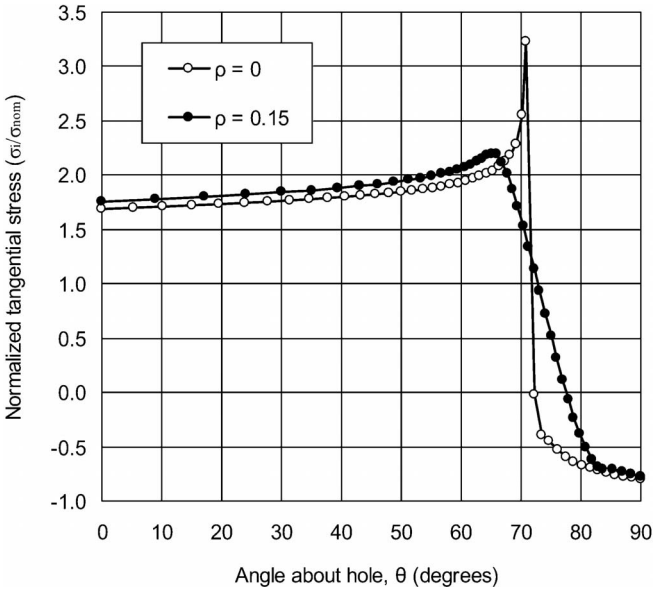

Fig. 14 Stress distributions about the basic stress-minimization optimal hole boundaries with and without a minimum-radius constraint, showing results when the load angle is perturbed $-5°$ away from the nominal orientation

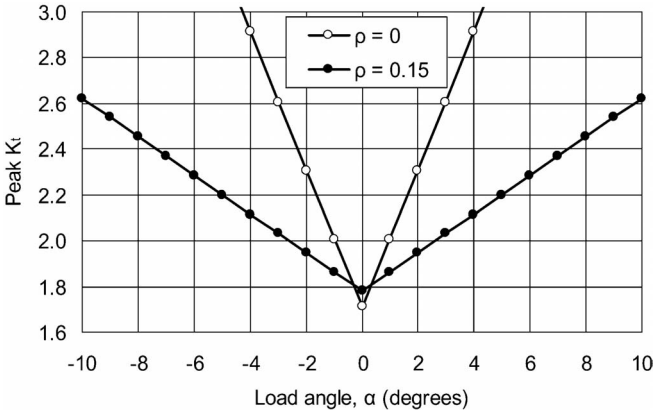

Fig. 15 K_t sensitivity curves for the basic stress-minimization optimal hole shapes with and without a minimum-radius constraint

The effect that the load angle has on the peak K_t is conveniently represented by the K_t-sensitivity curves shown in Fig. 15. As expected, the peak K_t is a minimum when $\alpha = 0°$, and linearly increases rapidly as the load angle varies away from this nominal value. It can be seen that when a minimum-radius constraint is applied, the K_t-sensitivity is decreased, however there clearly exists scope and benefit to reduce the sensitivity even further.

8 Illustrative example for the robust stress-minimization method

The aim here is to determine a robust stress-optimal hole shape that gives minimum K_t when the angular orientation of the remote load is expected to occur anywhere within a prescribed range. Here the analysis is demonstrated for the design range of $-5° \leq \alpha \leq +5°$. The total load-angle range was discretized into $1°$ increments from $-10°$ to $+10°$, and applied to the FE model as separate load cases, i.e. $m = 21$. During the optimization, the node movements

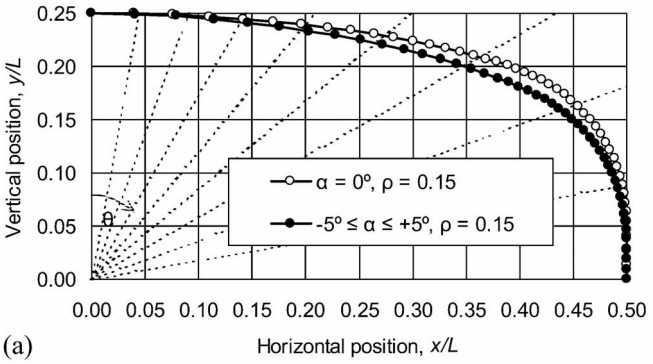

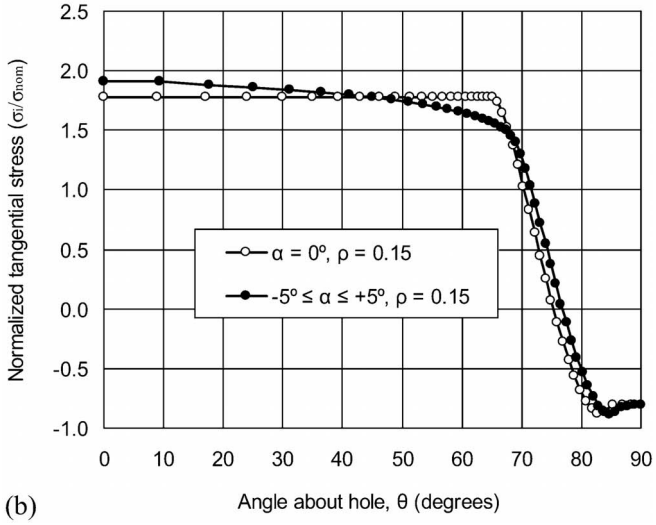

Fig. 16 Robust stress minimization results showing (a) optimal hole shapes and (b) stress distributions about the hole boundaries when the load angle is at the nominal orientation of $\alpha = 0°$

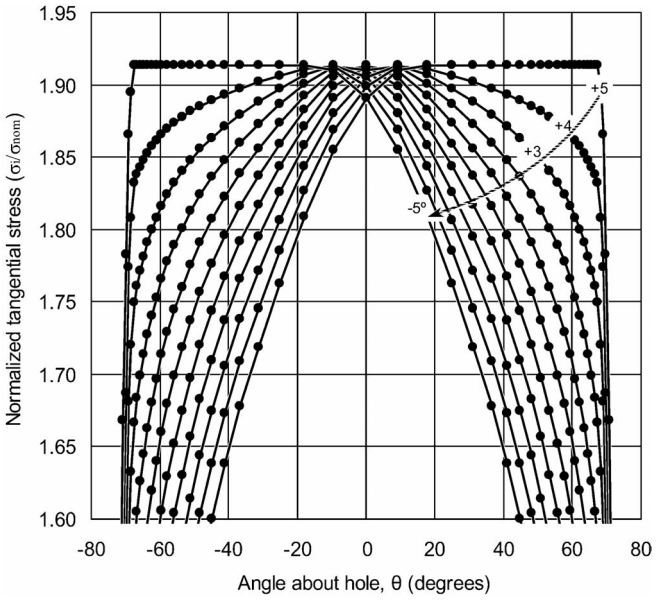

Fig. 17 Typical stress distribution about the robust stress-minimization optimal hole boundary for the $-5^\circ \leq \alpha \leq +5^\circ$ load range case, at increments of 1°

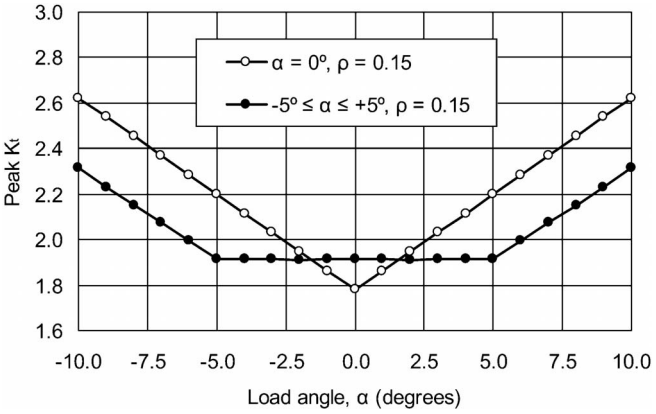

Fig. 18 K_t sensitivity curves for the robust and non-robust stress-minimization optimal hole shapes

for each position along the boundary were calculated in accordance with (2), with a minimum-radius constraint of $\rho = 0.15$.

The resulting shape is shown in Fig. 16(a), which also includes for comparison the basic optimal shape result for the nominal load angle of $\alpha = 0^\circ$. Figure 16(b) compares the stress distributions about these holes at the nominal load angle, and Table 1 summarizes peak K_t results.

Figure 17 reveals the stress distributions about the robust optimal hole for the $-5^\circ \leq \alpha \leq +5^\circ$ design-range case, showing typical results at 1° load-angle increments. It can be seen here that the magnitude of the peak stress for each load case within the $\pm 5^\circ$ range is the same irrespective of the load angle, however the location of the peak stress varies with load angle.

The corresponding peak K_t sensitivity curve is given in Fig. 18. It can be seen that the initial optimization objective, to obtain peak-stress uniformity for a continuous load-angle range has been accomplished. To the authors' knowledge, this is a unique characteristic of a local stress-concentrating detail that has not been achieved before. As expected, the minimum peak K_t achieved at $\alpha = 0^\circ$ is slightly higher than the non-robust shape, indicating that there is a trade-off between robustness and the minimum stress attainable. For load angles outside the $\pm 5^\circ$ design range, peak $K_t$increases as expected.

9 Illustrative examples for the non-robust and robust fatigue-damage-minimization methods

The aim here is to determine a robust optimal hole shape that gives minimum peak fatigue damage, and also compare it to the relative fatigue performance of the basic and robust stress-minimization shapes. Here the load-angle occurrence (α–N) distribution is the key input, since the peak fatigue damage accumulated is expected to vary depending on the how the orientation of the loading varies each cycle. Three α–N distributions are investigated here: (1) the non-robust baseline case where the α is fixed at a single orientation ($\alpha = 0^\circ$); (2) a robust case where α–N is uniformly distributed such that α has a equal probability of occurring anywhere between a given range of $-5^\circ \leq \alpha \leq +5^\circ$, as shown in Fig. 19; and (3) a robust case where α–N is normally distributed with a given average of $\alpha_{avg} = 0^\circ$ and standard deviation of $\alpha_{stdev} = 5^\circ$.

A stress-life (S–N) relationship typical of structural steel is specified, such that stress amplitudes of $0.9\sigma_u$ and $0.5\sigma_u$ result in fatigue failure at 1000 and 1 000 000 cycles respectively, where σ_u is the ultimate strength of the material (this was set equal to 3 times the applied remote stress range, i.e. $\sigma_u = 3\Delta\sigma_{nom}$). Hence, the S–N constants in (5) and (6) are $a = -0.0851$ and $b = 2.687$. The endurance stress limit was set as $\sigma_e = 0.5\sigma_u$. The fatigue damage at each position about the boundary was then calculated in accordance with (3)–(6). The total number of load cycles was arbitrarily chosen to be $n_{total} = 100\,000$.

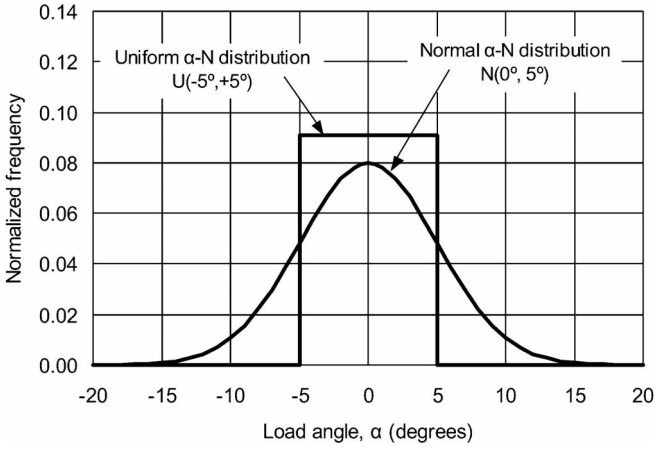

Fig. 19 Graph of normalized frequency for the uniform and normal α–N distributions that were investigated

9.1 Fatigue damage results for α fixed at a single load angle

Here it is assumed that the cyclic loading is always orientated precisely at $\alpha = 0°$ for all load cycles. The fatigue damage distribution about the basic stress minimization shape ($\alpha = 0°$, $\rho = 0.15$) from Sect. 7, is calculated here in accordance with (4)–(6). The resulting fatigue damage distribution (see Fig. 20) is uniform along the optimal boundary ($\Psi_f = 0.55\%$), and hence minimum. This is an expected result given that the simple fatigue model used herein only considers the free-boundary stress. Therefore, for the given fatigue model, the basic stress-minimization shape is also optimal for fatigue damage when the load angle is fixed at the same single orientation.

9.2 Fatigue damage results for a uniform α–N distribution

An optimal shape was determined here using the robust fatigue-damage gradient-less method ((3)–(6) and (8)) to optimize the shape for minimum peak fatigue damage. The load angle each cycle is assumed to occur uniformly over the range $-5°$ to $+5°$, notated as U($-5°$, $+5°$). Hence the load case array was selected to consist of discretized load angles of $\alpha = -5°, -4° \ldots +5°$ ($m = 11$), as shown in Fig. 21. The number of cycles applied to each load case is given by $n_j = n_{total}/m$ which is readily substituted into (4).

The robust fatigue-damage distribution is given in Fig. 22, and the optimal shape is shown later in Fig. 24. Also, a summary of the peak fatigue-damage results is given in Table 2. It can be seen that the distribution is uniform ($\Psi_f = 0.11\%$), and hence minimum.

For comparison, the fatigue-damage distributions about a basic ($\alpha = 0°$) and robust ($-5° \leq \alpha \leq +5°$) stress-minimization shape, under the same uniform α–N load distribution, is also given in Fig. 22. It can be seen that the optimal fatigue-damage solution provides a clear benefit compared to both the basic and robust stress-minimized hole shapes.

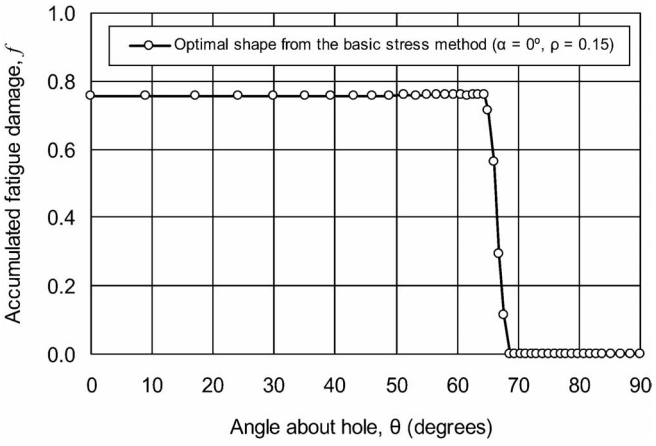

Fig. 20 Fatigue-damage distribution about the basic stress-minimization shape, when the α–N distribution is fixed at the nominal design angle ($\alpha = 0°$)

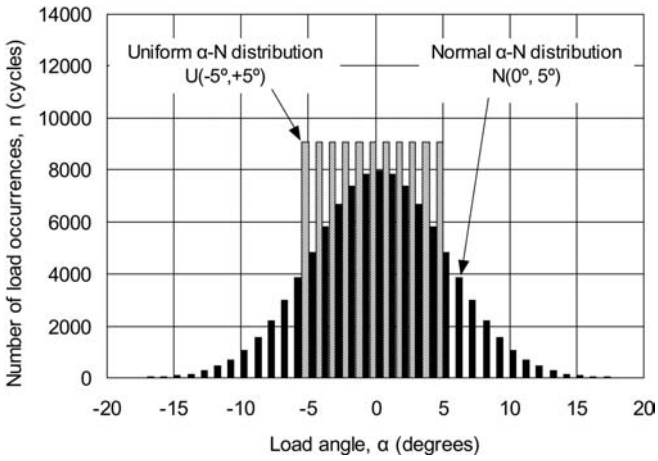

Fig. 21 Discretized load occurrences for the uniform and normal α–N distributions that were investigated

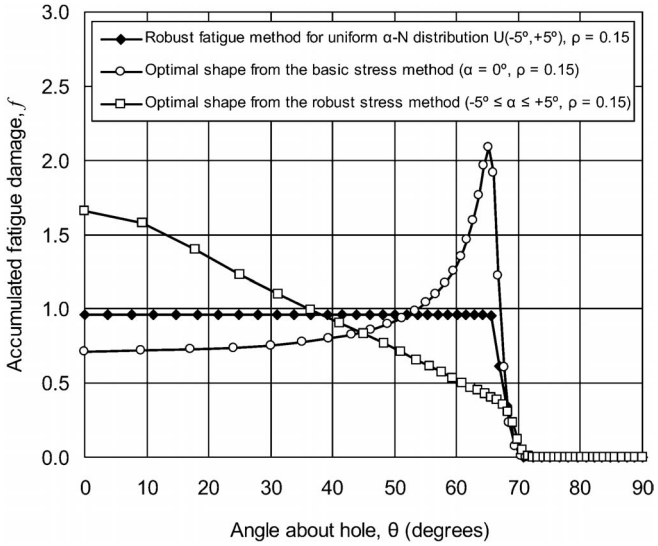

Fig. 22 Cumulative fatigue-damage results for a uniform α–N distribution U($-5°$,$+5°$), for the robust fatigue-optimized solution, as compared to the basic and robust stress-minimized shapes

9.3 Fatigue damage results for a normal α–N distribution

Here it is assumed that α–N is normally distributed about an average value of $\alpha_{avg} = 0°$ with a standard deviation of $\alpha_{stdev} = 5°$, notated here as N(0°, 5°). The load case arrays were selected to consist of discretized load angles of $\alpha = -20°, -19° \ldots +20°$ ($m = 41$) which is considered to represent the normal distribution faithfully (Fig. 21).

The resulting optimal hole shape is shown in Fig. 24. The fatigue-damage distribution (Fig. 23) is uniform, and hence minimum. This indicates that the initial stated

Table 2 Summary of peak fatigue-damage results for the robust fatigue-damage minimization optimal shapes for a 2 : 1 hole aspect ratio with a minimum-radius constraint of $\rho = 0.15$, as compared to the basic and robust stress-minimized shapes

Optimisation method	Load-angle occurrence (α–N) distribution	Convergence parameter Ψ_f	Peak fatigue-damage f (bold values represent optimal results)
Robust fatigue-damage minimization	Uniform, U(-5°, $+5^\circ$)	0.11%	**0.97**
	Normal, N(0°, 5°)	0.08%	**1.20**
Basic stress minimization ($\alpha = 0^\circ$)	Fixed at $\alpha = 0^\circ$	0.55%	**0.76**
	Uniform, U(-5°, $+5^\circ$)		2.08
	Normal, N(0°, 5°)		7.89
Robust stress minimization ($-5^\circ \leq \alpha \leq +5^\circ$)	Uniform, U(-5°, $+5^\circ$)		1.66
	Normal, N(0°, 5°)		1.52

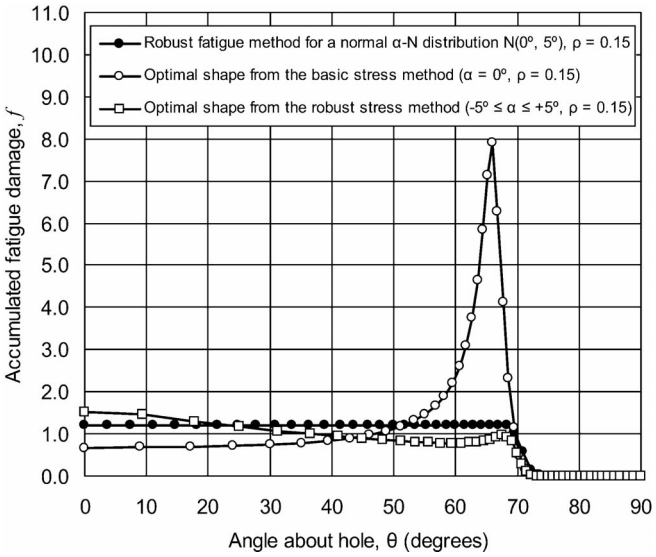

Fig. 23 Cumulative fatigue-damage results for a normal α–N distribution N(0°, 5°), for the robust fatigue-optimized solution, as compared to the basic and robust stress-minimized shapes

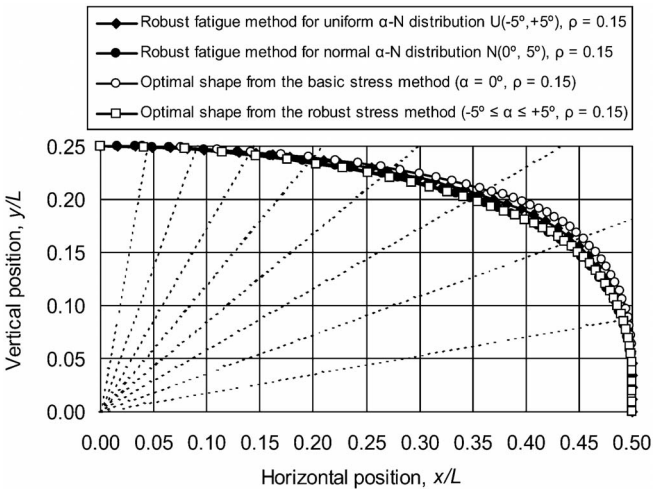

Fig. 24 Optimal hole shapes determined by the robust fatigue-damage-minimization method for when α–N is either uniformly or normally distributed, as compared to the basic and robust stress-minimized shapes

aim of the numerical algorithm has been achieved. By comparison, the shape from the basic stress optimization performs very poorly under this α–N distribution, with a very high peak fatigue damage. Conversely, the robust stress method shape performed reasonably well, with a peak fatigue-damage 27% higher than the optimal result.

The illustrative examples have clearly shown that there are very significant fatigue-life benefits to be gained by employing robust-fatigue shape optimization methods for notches with variable load conditions, as compared to the basic (non-robust) stress approaches that have historically been used in prior work.

10 Conclusion

An iterative 2D finite-element-based optimization procedure has been developed for notches, which incorporates robust design philosophies. Firstly, a robust stress method is developed that produces a notch shape that results in a minimum peak stress that remains constant for a continuous range of load orientations. Secondly, a robust fatigue-damage method is developed that produces a notch shape with minimum peak fatigue-damage for cyclic loads where the orientation of each load occurrence has a probabilistic distribution. Numerical examples are then given to demonstrate the method. These consider geometrically constrained holes in plates, where load alignment variability is present. For the conditions investigated it is shown that the robust optimization methods provide fatigue lives 2 to 8 times longer as compared to non-robust methods.

Further improvements may be made to the procedure by incorporating a more representative fatigue-damage model than the linear cumulative damage rule used in this paper. However, it is clearly shown in this work that accounting for variability in load orientations (or multiple load cases) can offer a large fatigue-life extension; this may be greater than that yielded by refining the fatigue-life model. Extension of the present numerical approach to 3D along with fatigue testing of the robust optimal shapes is planned to guide further development.

It is anticipated that the implementation of robust optimal notch shapes in metallic structures would result in reduced life-of-component costs through one or more of the following: more relaxed manufacturing tolerances; a common **robust** optimal notch shape that may be used in several structural variants; improved reliability of life assessments; and longer fatigue-life extension.

References

Baud, R.V. 1934: Fillet profiles for constant stress. *Prod Eng* (April), 133–134

Burchill, M.; Heller, M. 2004a: Optimal notch shapes for loaded plates. *J Strain Anal* **39**(1), 99–116

Burchill, M.; Heller, M. 2004b: Optimal free-form shapes for constrained holes in loaded plates. *(for publication in Int J Fatigue)*

Chandu, S.V.L.; Grandhi, V. 1995: General purpose procedure for reliability based structural optimization under parametric uncertainties. *Adv Eng Softw* **23**, 7–14

Chaperon, P.; Jones, R.; Heller, M.; Pitt, S.; Rose, F. 2000: A methodology for structural optimisation with damage tolerance constraints. *J Eng Fail Anal* **7**, 281–300

Dhir, S.K. 1981: Optimisation in a class of hole shapes in plate structures. *J Appl Mech* **48**, 905–908

Durelli, A.J.; Rajaiah, K. 1979: *Quasi-square hole with optimum shape in an infinite plate subjected to in-plane loading.* Oakland University ONR Report No. 49

Fanni, M.; Schnack, E.; Grunwald, J. 1994: Shape optimization of dynamically loaded machine parts. *Int J Press Piping* **59**, 281–297

Grunwald, J.; Schnack, E. 1997: A fatigue model for shape optimization. *Struct Optim* **14**, 36–44

Heller, M.; Burchill, M.; McDonald, M.; Watters, K.C. 2001: *Shape Optimisation of Critical Fuel Flow Vent Holes in the F-111 Wing Pivot Fitting.* DSTO-TR-1120, Defence Science and Technology Organisation, Melbourne, Australia

Herskovits, J.; Dias, G.P.; Mota Soares C.M. 1996: A Full Stress Technique for Structural Optimization. *Appl Math Comp Sci J Shape Optim Sci Comp* **6**(2), 303–319

Heywood, R.B. 1945: Photo-Elasticity and Design Problems (Part II). *Aircr Eng* **17**, 226–228

Kaye, R.; Heller, M. 1997: *Structural Shape Optimization by Iterative Finite Element Solution.* DSTO-RR-0105, Defence Science and Technology Organisation, Melbourne, Australia

Kristensen, E.S.; Madsen, N.F. 1976: On the Optimum Shape of Fillets in Plates Subjected to Multiple In-plane Loading Cases. *Int J Numer Methods Eng* **10**, 1007–1019

Mattheck, C.; Burkhardt, S. 1990: A new method of structural shape optimisation based on biological growth. *Int J Fatigue* **12**(3), 185–190

McDonald, M.; Heller, M.; Goldstraw, M.; Hew, A. 2001: *Robustness of the F-111 Wing Pivot Fitting Optimal Rework Shapes.* DSTO-TR-1121, Defence Science and Technology Organisation, Melbourne, Australia

Melchers, R.E. 2001: Optimality-criteria-based probabilistic structural design, *Struct Multidisc Optim* **23**, 34–39

Miner, M.A. 1945: Cumulative damage in fatigue. *Trans ASME* **67**, A159–A164

Neuber, H. 1969: Der zugbeanspruchte Flachstab mit optimalem Querschnittsübergang. *Forschung im Ingenieurwesen* **35**(1), 29–30

Parkinson, A.; Sorensen, C.; Pourhassan, N. 1993: A General Approach for Robust Optimal Design. *J Mech Des* **115**, 74–80

Phadke, M.S. 1989: *Quality engineering using robust design,* NJ: Prentice Hall

Roa, S.S. 1979: *Optimization Theory and Applications,* NJ: John Wiley Eastern

Schnack, E. 1979: An optimization procedure for stress concentrations by the finite element technique. *Int J Numer Methods Eng* **14**, 115–124

Schnack, E.; Sporl, U. 1986: A mechanical dynamic programming algorithm for structural optimisation. *Int J Numer Methods Eng*. **23**, 1985–2004

Taguchi, G.; Elsayed, E.; Hsiang, T. 1989: *Quality Engineering in Production Systems,* NY: McGraw-Hill

Vigdergauz, S.B; Cherkayev, A.V. 1986: A hole in a plate optimal for its biaxial tension-compression. *J Appl Math Mech* **50**(3), 401–404 (English Translation)

Waldman, W.; Heller, M.; Chen, G. 2001: Optimal free-form fillet shapes for tension and bending. *Int J Fatigue* **23**, 509–523

Waldman, W.; Heller, M.; McDonald, M.; Chen, G. 2002: Developments in rework shape optimisation for life extension of aging airframes. *3rd Australasian Cong. Appl. Mech.* World Scientific 695–702, Sydney, Australia

Waldman, W.; Heller, M.; Rose L.R.F 2003: *Shape optimisation of two closely spaced holes for fatigue life extension*. DSTO-RR-0253, Defence Science and technology Organisation, Melbourne Australia

Xie, Y.M.; Steven, G.P. 1992: *Optimal design of multiple load case structures using an evolutionary procedure,* Finite Element Analysis Research Centre, University of Sydney, Australia